Applied Acoustics 116 (2017) 70–81

Contents lists available at ScienceDirect

Applied Acoustics

journal homepage: www.elsevier.com/locate/apacoust

Measuring, modelling and optimising an embedded rail track

Yue Zhao [a,c,*], Xusheng Li [b,c], Qiang Lv [c], Honglin Jiao [c], Xinbiao Xiao [a], Xuesong Jin [a]

[a] State Key Laboratory of Traction Power, Southwest Jiaotong University, Chengdu 610031, China
[b] School of Economics and Management, Southwest Jiaotong University, Chengdu 610031, China
[c] Chengdu Xinzhu Road & Bridge Machinery Co. Ltd., Chengdu 611430, China

ARTICLE INFO

Article history:
Received 23 September 2015
Received in revised form 19 July 2016
Accepted 22 July 2016

Keywords:
Embedded rail
Wheel/rail rolling noise
Decay rate
Tramway
Frequency response function

ABSTRACT

A finite element (FE) model and a boundary element (BE) model have been developed to predict the decay rate, vibration and noise responses of an embedded rail track. These models are validated using measured results. The optimisation of the embedded rail track is conducted using these calculated models. The results indicate that the optimised cross-section of the gutter for the embedding rail can significantly reduce the radiated noise of the embedded rail track. The embedded rail track using the I-shaped cross-section gutter reduces the radiated noise of the track by at least by 3 dB(A). Furthermore, combining the material parameter optimisation with the gutter cross-section optimisation can further reduce the radiated noise of the embedded rail track. Increasing the Young's modulus of the rail pad in the embedded rail track with the I-shaped cross-section gutter can result in a radiated noise reduction of 4 dB(A).

1. Introduction

With the rapid development of urbanisation, urban transport problems have become an increasingly important issue. Urban railway transit has been encouraged because it can effectively solve the congestion of road traffic and is environmentally-friendly. Tramway rail systems on the surface are cost-effective [1] and often used to facilitate street running [2]; therefore, they are still applied in urban transit.

An embedded rail track is a type of tramway rail system. In this type of structure, rails are embedded in an elastomeric material, which performs well in isolating rail vibrations and reducing the radiated noise of the track. Embedded rail tracks with continuously supported rails have better dynamic track responses, better damping characteristics and provide a more favourable vehicle-track interaction compared to classic ballasted tracks [3]. Furthermore, through an analysis using a waveguide finite element and boundary element approach, it can be determined that the embedded rail track can emit a considerably lower noise level if it is appropriately designed [4]. For example, an optimised embedded rail track with a small rail profile can emit between 4 and 6 dB(A) less noise than a ballasted track [5]. However, the vibration and radiated noise of an embedded rail track is not always desired; an embedded rail track without optimisation emits between 1.5 and 3 dB(A) more noise than the ballasted track [5].

In recent years, an increasing number of embedded rail tracks have appeared in China. In this report, based on the vibration and noise measurements conducted on an embedded rail track in the Xinzhu rail transit industrial park located in Xinjin, Chengdu suburb, FE and BE models are developed to calculate the vibration and noise characteristics of the embedded rail track. Using these models, material parameters and a gutter cross-section of the embedded rail track are optimised with respect to its vibration and radiated noise.

2. Embedded rail track

For traditional ballasted tracks and slab tracks, the rails are discontinuously supported by rail fasteners whereas for embedded rail tracks, a pair of rails are continuously supported. As indicated in Fig. 1, the 59R2 groove rails are placed in two longitudinal rectangular gutters created in the slab, and the rails are embedded with a type of elastomer consisting of rubber crumbs and polyurethane. PVC tubes placed on both sides of the rail web are used to reduce the amount of embedding elastomer material. Tube holders and elastic wedges on the two sides of the rail bottom at discontinuous equidistant points are used to hold the tubes and adjust the rail gauge.

* Corresponding author at: State Key Laboratory of Traction Power, Southwest Jiaotong University, Chengdu 610031, China.
E-mail address: zhaoyue@my.swjtu.edu.cn (Y. Zhao).

http://dx.doi.org/10.1016/j.apacoust.2016.07.021
0003-682X/

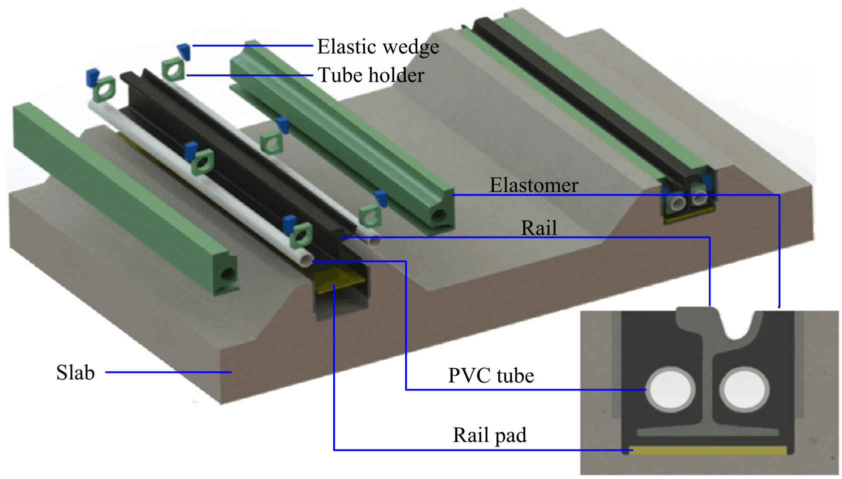

Fig. 1. Embedded rail track.

3. Experimental analysis of the embedded rail track

3.1. Vibration characteristics of the track

Measurements of the embedded rail track were conducted on the Xinzhu rail transit industrial park located in Xinjin in the Chengdu suburb. According to the standard ISO 7626-5 [6], the frequency response functions (FRFs) of the track were measured using a hammer excitation. As indicated in Fig. 2, accelerometers were fixed on the rail head, elastomer and slab surface using AB glue in the vertical direction. Therefore, the response of the elastomer at higher frequencies can be attenuated by the mounting. Additionally, the accelerometer mass is 180 g so that the accelerometer resonance with respect to the elastomer affects the accuracy of the measurement to a certain extent. The FRFs of the rail head, elastomer and slab surface were measured when the hammer was used to knock on the rail head in the vertical direction.

Additionally, according to the European standard EN 15461 [7], the vertical FRFs of the rail head along the longitudinal direction of the track were measured to assess the vibration decay rates of the embedded rail track. The decay rate influences the decay of vibration along the track and determines the length of the excited track; as the length of the vibrating track increases, more noise is radiated [2].

As indicated in Fig. 3, the thick black line represents the rail, the rectangular shaded blocks under the thick black line represent the slabs, and the red circle represents the measuring point of the accelerometer. The black arrows in Fig. 3 represent the positions of the hammer impacting on the rail. The accelerometer was fixed on the rail head to measure the vertical acceleration. The distribution of the hammer hitting points has three categories: the spot, the near field and the far field. Their intervals are indicated by the blue numbers above the arrows.

The measured FRFs were expressed in the form of a one-third octave band spectra, and the decay rates in each one-third octave band can be evaluated using the formula [8] as follows:

$$DR = \frac{4.343}{\sum_{i=0}^{i=29} \frac{|A(x_i)|^2}{|A(x_0)|^2} \Delta x_i} \tag{1}$$

where DR is the decay rate, which is measured in dB/m; $A(x_i)$ is the measured FRF when the hammer is applied at the position of arrow i; and Δx_i is the distance between adjacent forcing points associated with position i, which is measured in m. Fig. 4 depicts the measured FRFs of the embedded rail track. It can be seen that the measured rail FRF (black solid line) above 100 Hz increases to more than 0.1 m/s^2/N, and it has the highest amplitude in this frequency range. The first two resonances occur at approximately 160 Hz and 630 Hz. Additionally, the measured elastomer FRF (red[1] dashed line) has two peaks at approximately 160 Hz and 630 Hz. The peak at 160 Hz of the elastomer reaches more than 0.6 m/s^2/N, and it is more significant than that of the rail, which is partly due to the resonance of the accelerometer with respect to the elastomer, as indicated in Fig. 5. The modal analysis results of the FE model for the track, including the accelerometer, indicate that the accelerometer and the elastomer have resonant frequencies in the frequency range from 160 Hz to 230 Hz. However, the elastomer peak at 630 Hz and the elastomer FRF amplitude in the higher frequency range are smaller than those of the rail. At approximately 630 Hz, the local elastomer vibration slightly increases along with the rail head. The vibration response of the elastomer after 160 Hz has a tendency to decline because of the damping effect of the elastomer in the higher frequency range. Additionally, the amplitude of the elastomer can largely isolate the vibration propagation from the rail to the slab.

Fig. 6 illustrates the measured decay rate of the embedded rail. It can be seen that the decay rate of the embedded rail is relatively higher in the frequency bands below 100 Hz and above 1000 Hz whereas it drops to less than 1 dB/m in the range from 100 Hz to 1000 Hz. The vibration decays rapidly along the track longitudinal direction in the frequency bands below 100 Hz and above 1000 Hz whereas the vibration propagates freely along the track longitudinal direction in the frequency range from 100 Hz to 1000 Hz; therefore, this embedded rail track vibrates and radiates noise easily in the frequency range from 100 Hz to 1000 Hz.

3.2. Vibration and noise characteristics during tram running

Furthermore, when a tram was running on an embedded rail track, the accelerations of the embedded rail track and wheel/rail rolling noise were measured. The accelerometers were fixed on a side of the rail head along with the elastomer and the slab surface using AB glue to measure the vertical responses. The accelerometer mass is 60 g (lighter than that used in the FRF measurements), which results in a higher resonance frequency of the accelerometer with respect to the elastomer, i.e., approximately 300 Hz. Additionally, a microphone was placed in the centre of the tram bogie area to measure the wheel/rail rolling noise when the tram was run-

[1] For interpretation of colour in Figs. 4, 27–30, the reader is referred to the web version of this article.

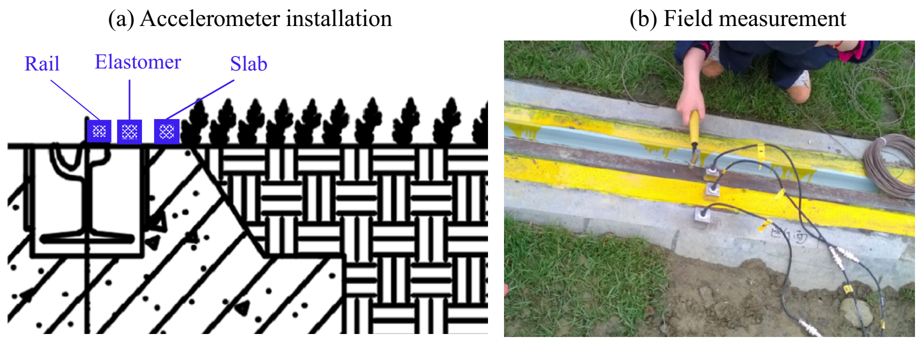

Fig. 2. FRF measurements using hammer excitation.

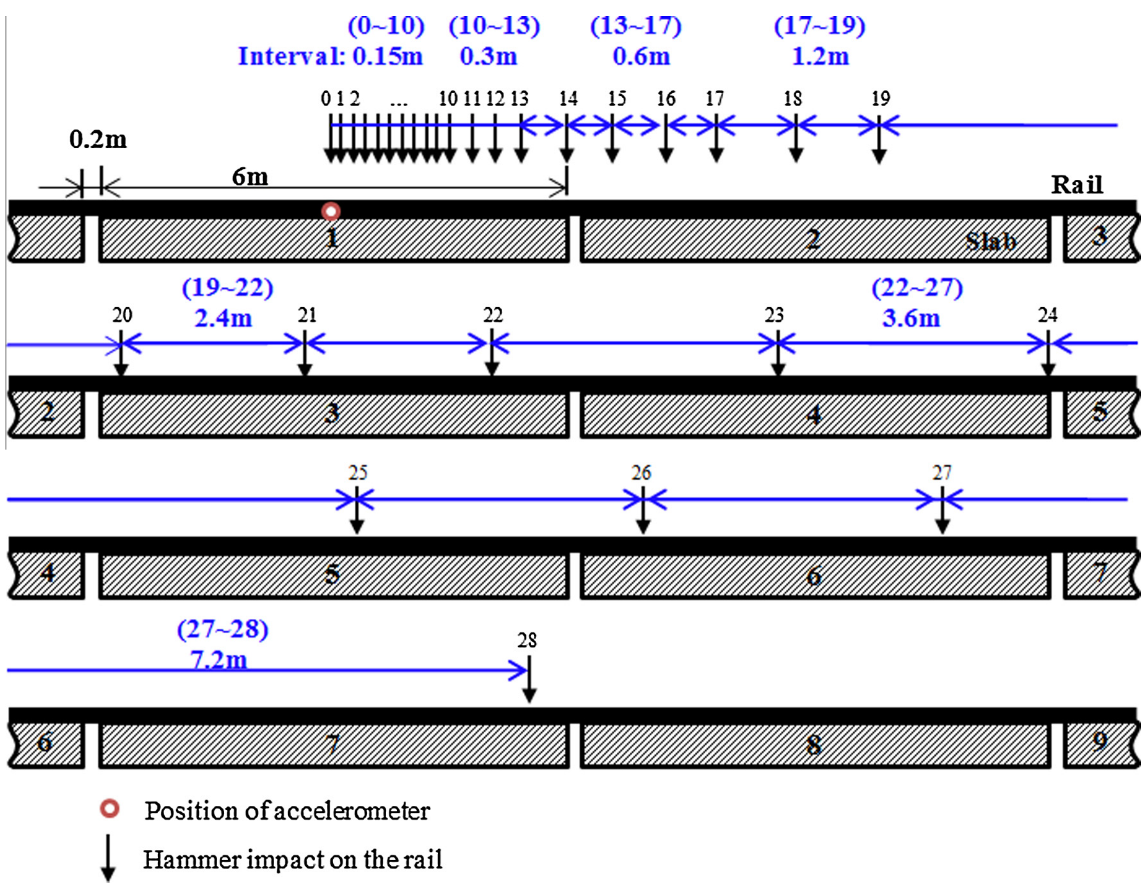

Fig. 3. Exciting and measuring points.

ning, and the distance between the microphone and the rail head was approximately 0.3 m.

Fig. 7 illustrates the measured acceleration spectra of the embedded rail track when the tram was running at 60 km/h. The averaging time covers the entire tram passing by the measuring point. By comparing the spectra with the measured FRFs of the embedded rail track, it can be determined that the distribution of the acceleration spectra is similar to that of the FRFs. The rail acceleration is dominant in the frequency band above 125 Hz and appears to peak near 30 dB in the range from 800 Hz to 1000 Hz whereas the elastomer acceleration is dominant in the frequency band below 800 Hz, and it vibrates more strongly than the rail in this frequency band, especially in the range from 400 Hz to 500 Hz, where it reaches 35 dB, which is 12–14 dB more than that of the rail because the intensive local vibration modes of the elastomer in this frequency range can be easily excited by the tram moving. The slab acceleration is considerably lower than that of the rail and the elastomer in the entire frequency band. Furthermore, the elastomer can largely isolate the vibration propagation from the rail to the slab when a tram is running over the track.

Fig. 8 depicts the measured sound pressure spectrum and the overall sound pressure level of the wheel/rail rolling noise when the tram is running at 60 km/h. It can be seen that the overall sound pressure level of the wheel/rail rolling noise is 98.8 dB(A), which is obtained by summing the wheel/rail rolling noise spectrum in the frequency band of 80–4000 Hz. The noise reaches its highest levels between 400 Hz and 1000 Hz. By comparing the wheel/rail rolling noise spectrum with the acceleration spectra of the embedded rail track, it should be noted that the wheel/rail rolling noise spectrum presents two peaks at 400 Hz and 800 Hz. The

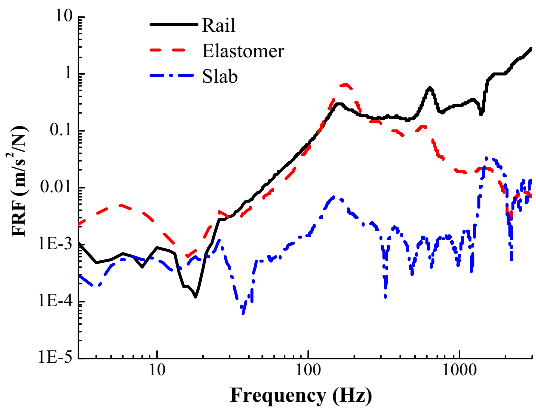

Fig. 4. Measured FRF of the embedded rail track.

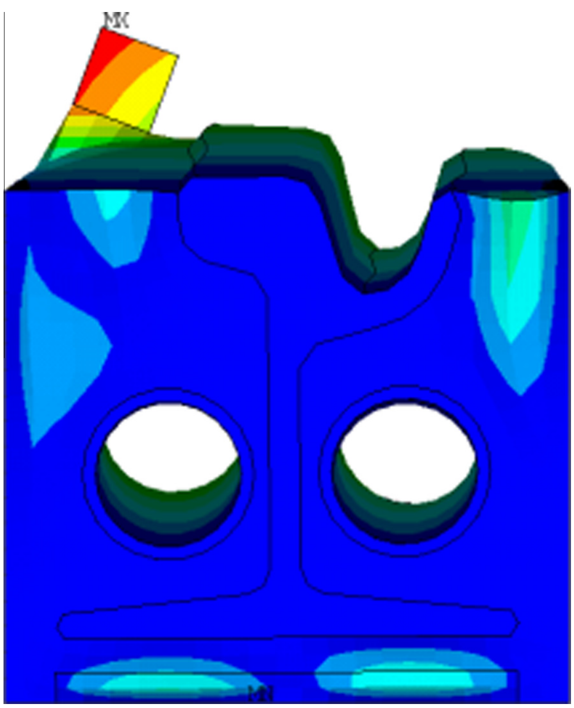

Fig. 5. Mode shape of the track and the accelerometer at approximately 171 Hz.

noise peak at 400 Hz is most likely caused by the radiated noise of

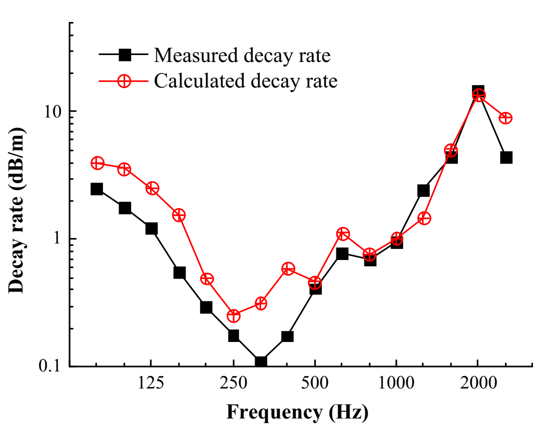

Fig. 6. Measured decay rate of the embedded rail track.

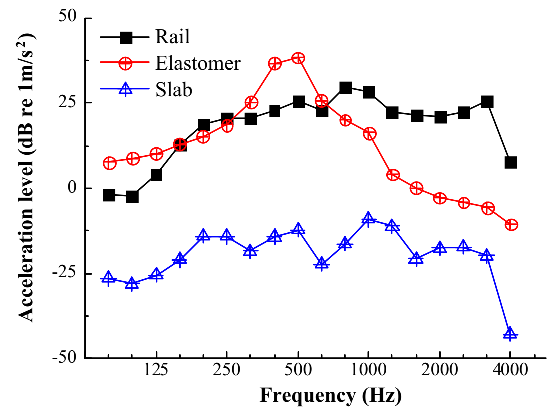

Fig. 7. Measured vertical accelerations of the embedded rail track when the tram is running at 60 km/h.

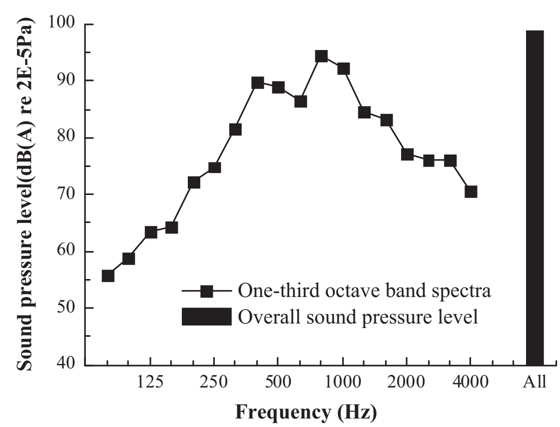

Fig. 8. A-weighted sound pressure level measured inside the bogie when the tram is running at 60 km/h.

the elastomer, and the noise peak at 800 Hz is most likely caused by the radiated noise of the rail. Therefore, eliminating the peaks of the rail and the elastomer may effectively reduce the radiated noise of the embedded rail track.

Additionally, it should be noted that the track decay rate is relatively low in the frequency band of 100–1000 Hz (see Fig. 6) whereas the rail and elastomer accelerations are relatively high in this frequency range. The track decay rate in this frequency range has a considerable influence on the vibration characteristics of the embedded rail track. The lower decay rate will result in a longer track structure vibrating and radiating noise, and properly increasing the decay rate in this frequency range will be beneficial to the rail vibration attenuation in the longitudinal direction of the track and reduce the radiated noise from the embedded rail track.

4. Modelling

4.1. Model to calculate the decay rate

The decay rate is a key factor that influences the vibration and radiated noise of the embedded rail track. For traditional tracks, because discontinuous rail pads provide the rails with elastic support, the decay rate is primarily influenced by the stiffness and damping of the rail pads. Similarly, for the embedded rail track, the elastic support for the rails is mostly provided by the elastomer in the gutters and the continuous rail pads; thus, the decay rate of the embedded rail is primarily influenced by the stiffness and damping of the elastomer and the rail pads. Therefore, a FE model of the embedded rail track (see Fig. 9) only considering the structural characteristics in the gutter is developed to predict the decay rate. It ignores the effects of the tube holders and the elastic wedges at the equidistant discontinuous points. The length of the considered track is 30.8 m, and the element size in the length-wise direction is 0.05 m, which is a result of a compromise selection between numerical accuracy and computational efficiency. Fig. 10 depicts the influence of the measurement length of the rail on the measured decay rate. It can be seen that the decay rates are close when the measurement lengths of the rail are greater than 14.4 m whereas the decay rates are quite different when the measurement lengths of the rail are shorter; therefore, a length of 30.8 m (equal to the length of five slabs) for the FE model has been selected. In this model, the boundary of the rectangular gutter is assumed to be fixed, and the track ends in the length-wise direction are assumed to be free. The length of the FE model is sufficiently long; however, the free boundary condition can cause reflections from the rail ends. A unit force is applied at the middle point of the model, i.e., at the rail head in the vertical direction to excite the track system. The accelerations at the different response points on the rail head are used to calculate the decay rate, and the response points are the same as the black arrows in Fig. 3. The calculation method of the decay rate refers to formula (1).

The material parameters used in this model are listed in Table 1, which were obtained from handbooks and specifications from the supplier. However, the Young's modulus of the elastomer and the

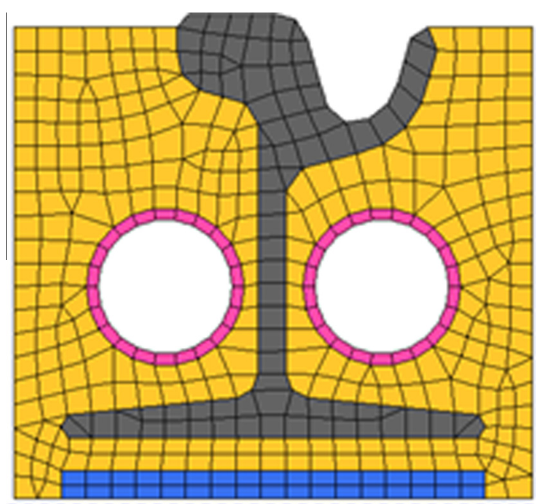

Fig. 9. FE model used to calculate the decay rate.

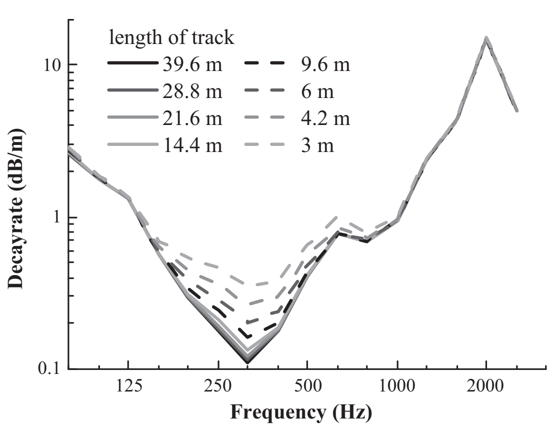

Fig. 10. Influence of the measurement length of the rail on the decay rate.

Table 1
Material parameters used in the FE models of the embedded rail structure.

Material	Young's modulus (MPa)	Poisson's ratio	Density (kg/m^3)	Damping loss factor
Rail	2.1e5	0.3	7850	–
Elastomer	5.0	0.45	1000	0.15
Rail pad	2.0	0.44	800	0.15
PVC tubes	3.14e3	0.35	1350	–
Slab	3.6e4	0.2	2400	–
Self-compacting concrete	3.25e4	0.2	2400	–

rail pad, which depend on several operational conditions, were tuned in such a way that the first two measured and predicted resonance frequencies agreed as closely as possible [5].

Fig. 11(a) illustrates the measured and calculated FRFs of the rail in the vertical direction. The calculated FRF of the rail is extremely consistent with the measured one, and the first two resonant frequencies of the calculated result, i.e., 180 Hz and 620 Hz, approximately agree with those of the measured one. Fig. 11(b) depicts the measured and calculated FRFs of the elastomer in the vertical direction. It can be seen from Fig. 11(b) that the first resonant frequency of the calculated result is 180 Hz, which approximately agrees with that of the measured one. The calculated FRF of the elastomer above 300 Hz is considerably greater than the measured result because the measured response of the elastomer at higher frequencies is attenuated by the mounting of the accelerometer. The comparison of the measured and calculated FRFs of the rail and elastomer demonstrates that the Young's modulus of the elastomer and the rail pad are set adequately in this FE model.

Furthermore, the comparison between the measured and the calculated decay rate of the embedded rail track is depicted in Fig. 6. It can be seen that the calculated decay rate is quite close to the measured one, especially in the higher frequency band. The calculated decay rate is slightly larger than the measured one, which is most likely due to the effect of the boundary condition of this FE model. Although a few differences exist in the two curves, the calculated decay rate can still reflect the vibration decay characteristics of the embedded rail track, and the FE model can thus be used to optimise the decay rate of the embedded rail track.

4.2. Theoretical method used to calculate vibration and noise

At usual speeds (typically 60 km/h), tram noise primarily results from the wheel/rail rolling noise. This is caused by the vibration and subsequent sound radiation of the tram wheels and the embedded rail track. The vibration is induced by the surface roughness in the contact patch between the wheel and the rail [5]. The calculation of the wheel/rail rolling noise of the tram and embedded rail track refers to a model originally presented by Remington [9]. However, the radiated noise of the wheels was not considered in the calculation of this study. The calculated sound pressure below only represents the noise radiated from the embedded rail track because it can be seen from the measured noise spectrum and the track vibration spectra that the measured noise reaches its highest levels between 400 Hz and 1000 Hz, which is most likely caused by the noise radiated by the track, whereas the noise radiated by the wheels typically dominates in the higher frequency range. Furthermore, the vibration responses of the tram wheels were not measured; thus, the predicted model of the wheel noise was not validated.

Based on the calculation method for the radiated noise from the embedded rail track, the input is the combination of the wheel and

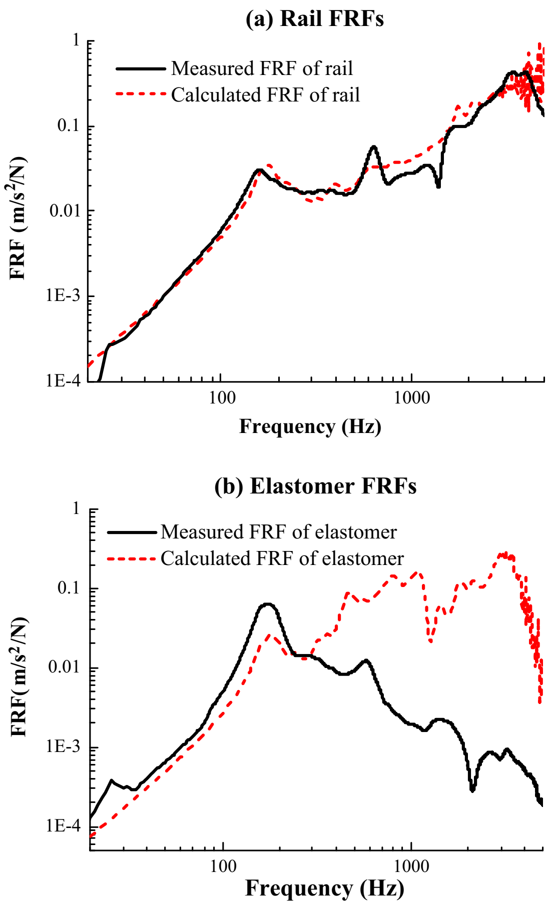

Fig. 11. Comparison of the measured and calculated FRFs.

rail roughness through the contact filtering. The contact forces of the wheel/rail are calculated using the compound roughness and the wheel, rail, contact receptances (transfer function from the force to the displacement). A FE model of the resilient wheel with a 660 mm diameter is used to calculate the wheel receptance, and an 18.4-metre-long FE model of the embedded rail track considering the structural characteristics of the gutter with a rectangular cross-section, slab and self-compacting concrete layer under the slab is used to calculate the rail receptance and track vibrations. The length of the track model is a compromise selection between numerical accuracy and computational efficiency, and the influences of the model length on the rail receptance and track vibrations are discussed in detail in Section 4.3. The calculated track vibration is used as the boundary condition for the BE model of the track to calculate the track noise radiation. Through propagation, the sound pressures at certain receiver locations are obtained.

The contact filter effect between the wheel and the rail in this model can be determined using an analytical model developed by Remington [10]: the shape of the contact zone is simplified as a circle contact patch with a radius γ, and the degree of correlation between the roughness across the width of the contact zone at a given wavenumber is described by α. A linearised Herzian contact spring with stiffness k_H is used to describe the contact between the wheel and the rail. The values of γ, α and k_H are listed in Table 2.

Fig. 12 depicts the wheel roughness spectrum and the rail roughness spectrum used in this model. The rail roughness spectrum was obtained through the measurement in the field whereas the wheel roughness spectrum is a statistical result of wheels with off-tread braking systems. The wheel/rail contact force can be calculated as follows:

Table 2
Parameters used to calculate the wheel/rail contact force.

Parameter	Value
α	1
γ	5.526e−3 m
k_H	1.18e9 m/N

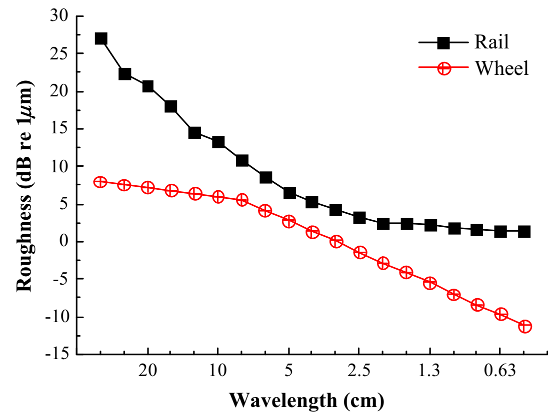

Fig. 12. Wheel roughness spectrum and rail roughness spectrum.

$$F = -\frac{R}{\alpha_W + \alpha_R + \alpha_C} \tag{2}$$

where F is the wheel/rail contact force; R is the compound roughness spectrum; and α_W, α_R and α_C are the wheel, rail and contact receptance, respectively. The receptances of the wheel and the rail were calculated using the FE model of the wheel and the track excited by the unit force, and the contact receptance α_C equals $1/k_H$. Fig. 13 illustrates the receptances of the wheel, rail and the contact spring used to calculate the wheel/rail contact force.

4.3. Model to calculate vibration and noise

As indicated in Fig. 14, the FE model analysis considers the structural characteristics of the gutter with a rectangular cross-section, slabs, and self-compacting concrete layer under the slabs while ignoring the structural characteristics of the soil because the radiated noise of the structures inside the gutter is significant, and the exposed slab surfaces near the gutter have a certain influence on the radiated noise whereas the radiated noise of the soil is

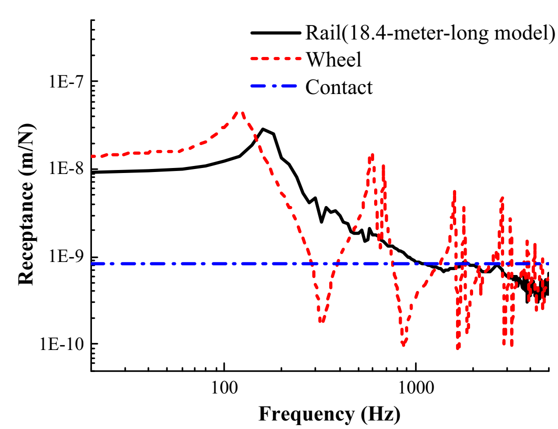

Fig. 13. Receptances of the wheel, rail and contact spring.

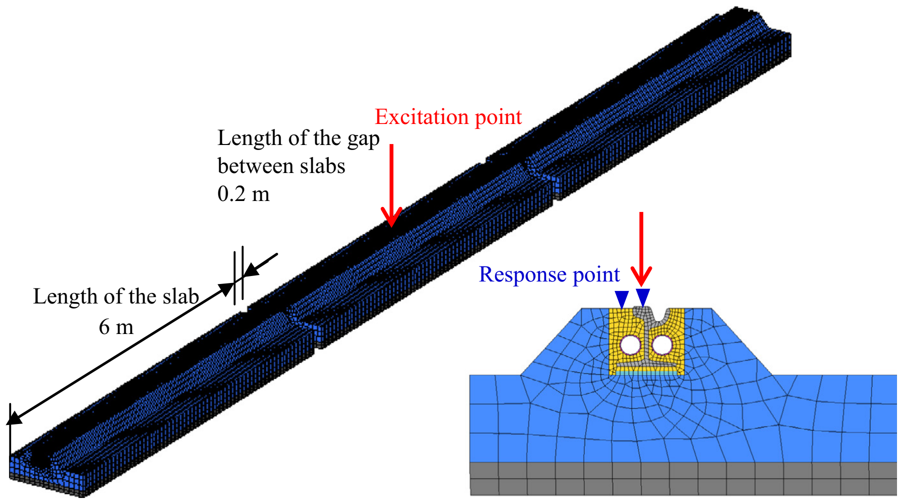

Fig. 14. FE model used to calculate vibration when the tram is running.

nearly negligible. This FE model only considers half of the track structure, which is assumed to be symmetrical. The bottom of the self-compacting concrete layer is assumed to be fixed in this model. The material parameters used in this model are listed in Table 1.

The length of the FE model is a key factor that influences the numerical accuracy and computational efficiency. The rail receptances calculated using the 6-metre-long FE model (equal to the length of one slab), 18.4-metre-long FE model (equal to the length of three slabs) and 30.8-metre-long FE model (equal to the length of five slabs) are compared in Fig. 15. It can be seen that the rail receptance calculated by the 6-metre-long FE model appears in small peaks in the frequency range from 200 Hz to 1000 Hz, which is caused by the reflections of the rail response from the rail ends because the 6-metre-long FE model is not long enough to handle the wave decay. However, the rail receptances calculated using the 18.4-metre-long FE model and the 30.8-metre-long FE model are significantly smoother in the frequency range from 200 Hz to 1000 Hz, and the rail receptance calculated using the 18.4-metre-long FE model is mostly consistent with that calculated using the 30.8-metre-long FE model.

Furthermore, the calculated wheel/rail contact force is applied at the middle point of the model, i.e., at the rail head in the vertical direction of each FE model to predict the vibration responses of the track when the tram is running at 60 km/h. Fig. 16 depicts the measured and calculated accelerations of the embedded rail track at a contact point. Therefore, the measured data, whose averaging time

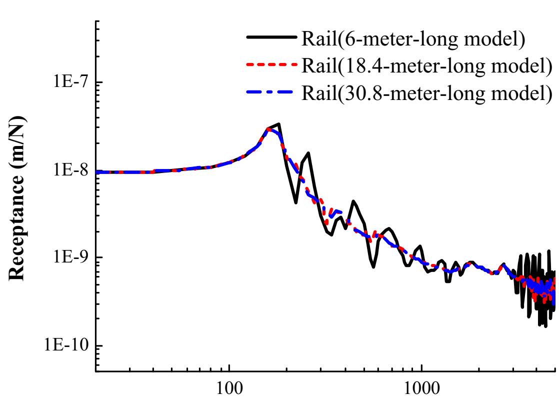

Fig. 15. Comparison of the rail receptances calculated using FE models with different lengths.

covers one wheel rolling over the measuring point, is selected to make a comparison. It can be seen that the rail and elastomer accelerations calculated using the three FE models with different lengths are mostly consistent. Additionally, by comparing the measured data with the calculated results, the calculated rail acceleration is in agreement with the measured one below 800 Hz whereas the calculated result overestimates the rail acceleration in the higher frequency band, and a similar phenomenon appears in the calculated and measured accelerations of the elastomer. There are two possible causes of this phenomenon. First, the bottom of the track model is assumed to be fixed; however, in the actual track structure, there is a deformable foundation below the track, which has a certain vibration-damping effect, and it is not considered in this model. Secondly, the contact damping of the wheel-rail is not considered in this model. Additionally, the mounting of the accelerometer on the elastomer is an important cause for the attenuation of the measured elastomer acceleration in the higher frequency band. Therefore, the calculated elastomer acceleration is higher than the measured one in the higher frequency band.

The BE model used to calculate the radiated noise of the track includes the surface of the rail head, elastomer and slab exposed in the air, which are the primary structures radiating noise outwards. Fig. 17 depicts the sound pressure spectra (four curves) and the overall sound pressure levels (four bars) of the measured wheel/rail rolling noise and the calculated track noise using the models with different lengths when the tram is running at 60 km/h, and the calculated results are the sound pressure levels at the middle point of the track and 0.3 m above the contact point.

Comparing the three calculated curves and the three calculated bars in Fig. 17, there are small differences between the sound pressure results calculated using the models with different lengths. The sound pressure calculated using the 6-metre-long model is slightly greater than that calculated using the longer length models in the frequency range from 250 Hz to 1000 Hz. The reflections of the rail response from the rail ends are most likely the reason for the greater sound pressure obtained in this frequency range. The calculated overall sound pressure levels using the 6-metre-long model, 18.4-metre-long model, 30.8-metre-long model are 99.5 dB(A), 97.8 dB(A), 97.7 dB(A), respectively. It can be concluded that the radiated noise calculated using the 18.4-metre-long model and the 30.8-metre-long model are mostly consistent whereas using the 6-metre-long model to conduct the calculation will lead to a slight overestimation in the radiated noise.

Additionally, when comparing the measured sound pressure spectrum, the overall sound pressure level obtained by the calcu-

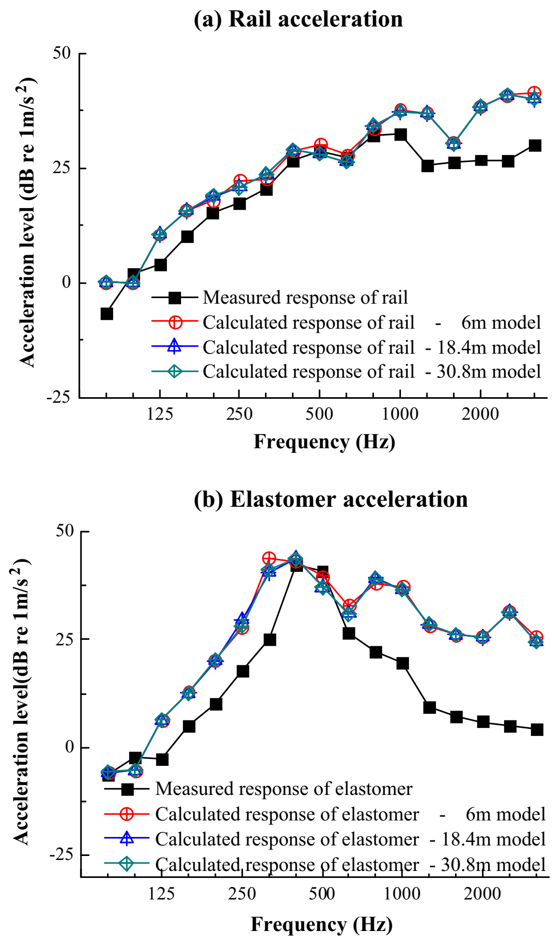

Fig. 16. Measured and calculated accelerations of the embedded rail track.

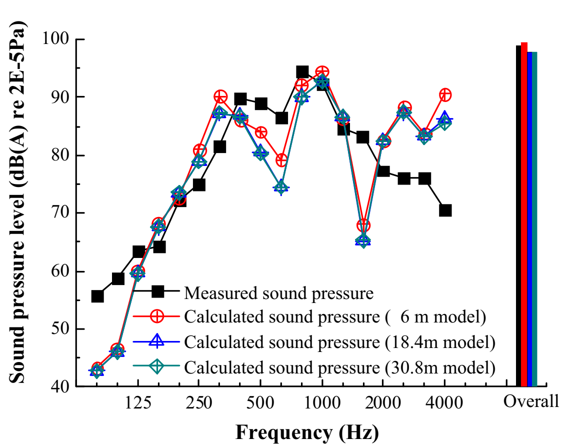

Fig. 17. Measured and calculated sound pressure level when the tram is running at a speed of 60 km/h.

lated sound pressure spectrum and the overall sound pressure level (18.4-metre-long model) in Fig. 17, the overall sound pressure level obtained with the calculated noise above the contact point is 97.8 dB(A), as indicated by the blue bar. It is not influenced by the decay rate and slightly lower than the measured one, as indicated by the black bar. Furthermore, the calculated sound pressure spectrum is close to the measured one in the frequency range from 160 Hz to 1000 Hz, and the frequency band of the sound pressure peak of the calculated result is essentially the same as that of the measured result. Additionally, a few differences exist between the two curves in the higher frequency bands. There are two reasons for resulting in these differences. One reason is that the calculated result does not contain the wheel radiated noise, and the other is that the overestimation of the calculated track accelerations leads to an increase in the calculated noise in the higher frequency band. Generally, the calculated sound pressure level spectrum can reflect the noise characteristics of the wheel/rail rolling noise, and the predicted model can be adequately used to optimise the noise performance of the embedded rail track.

It can be concluded from Figs. 15–17 that the 18.4-metre-long FE model is sufficiently long to obtain a relatively accurate result and simultaneously save computing time. Therefore, the 18.4-metre-long FE model (see Fig. 14) and the corresponding BE model are used to calculate the track vibration and noise below.

5. Optimisation of the embedded rail track

The radiated noise of the embedded rail track, which is an important part of the wheel/rail rolling noise of the tram and embedded rail track, can be optimised through a numerical analysis using the 18.4-metre-long model in this report. The following optimisation focuses on the rail and elastomer vibration at the contact point as well as the track radiated noise above the contact point. The optimisation does not include the effects of the decay rate on the radiated noise during a tram pass-by.

The radiated noise is related to the vibration characteristics of the embedded rail track. Reducing the vibration level of the embedded rail track in the frequency range from 100 Hz to 1000 Hz will be beneficial to noise reduction. The following optimisations are performed using two approaches: changing the material parameters and changing the gutter cross-section.

5.1. Material parameters optimisation

Certain material parameters of the embedded rail track, such as the rail, slab and self-compacting concrete, were considered to be constant in the current optimisation whereas the material parameters of the elastomer and the rail pads were optimised in a relatively wide range. The material parameters of the elastomer and the rail pads have significant effects on the vibration and noise characteristics of the embedded rail track. Therefore, the material parameters of the elastomer and the rail pads are initially optimised.

Using the calculated model described in Section 4.1, Fig. 18 depicts the decay rate of the embedded rail (only considering the structure in the gutter) with different values of Young's modulus

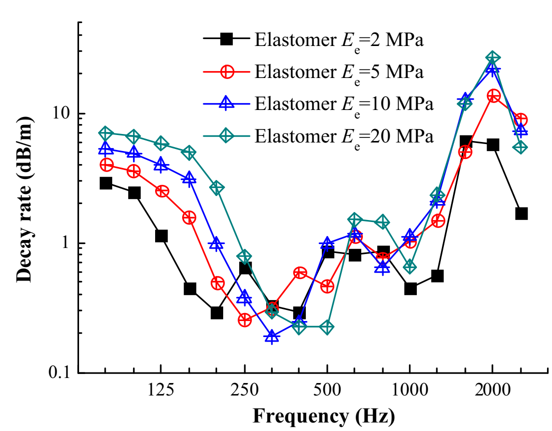

Fig. 18. Decay rate of the embedded rail for different E_e.

for the elastomer (called E_e below). The value of E_e used in the current model of the embedded rail structure is 5 MPa, which is tuned based on the measured FRF of the rail. It can be seen that E_e has a significant influence on the decay rate, the peak frequencies of the decay rate move towards higher frequency bands with the increase of E_e, the decay rate increases with an increase in E_e in the frequency range below 250 Hz and above 1000 Hz, an increase in the decay rate below 250 Hz is approximately between 2 and 4 dB/m when E_e increases from 2 MPa to 20 MPa, and the increase above 1000 Hz is considerably more significant. However, the decay rate decreases with an increase in E_e in the frequency band of 315–500 Hz. In this frequency range, the track vibrates and radiates noise significantly; therefore, increasing E_e will lead to the vibrating and radiating noise of a longer embedded rail in this frequency range.

Figs. 19 and 20 depict the rail accelerations and elastomer accelerations of the embedded rail track (consider the structure in the gutter, slab and self-compacting concrete layer under the slab) for different E_e. They were obtained using the calculated model described in Section 4.3. It can be seen that E_e has a slight influence on the rail acceleration, the rail vibration decreases slightly with an increase in E_e in the frequency band below 160 Hz, and the rail vibration increases slightly with an increase of E_e in the frequency band of 160–250 Hz. However, E_e has a significant influence on the elastomer acceleration, and the peak frequencies of the elastomer acceleration move towards the higher frequency band with an increase of E_e. Although the elastomer vibration decreases with an increase of E_e in the frequency band below 250 Hz, the elastomer vibration increases significantly with an increase in E_e in the frequency band above 500 Hz. The increase in the elastomer acceleration is approximately more than 10 dB when E_e increases from 2 MPa to 20 MPa.

Additionally, using the noise calculated model described in Section 4.3, the sound pressure spectra of the embedded rail track for different E_e are calculated when a tram is running at 60 km/h, as indicated in Fig. 21. It can be seen from Fig. 21 that the sound pressure spectra of the embedded rail track vary with an increase in E_e in a similar pattern to that of the rail and elastomer vibration. In the frequency band of 400–630 Hz, the vibration of the elastomer increases with an increase of E_e; therefore, the sound pressure of the embedded rail track also increases significantly with an increase in E_e in this frequency band. When E_e equals 10 MPa and 20 MPa, the sound pressure has a high peak at approximately 400 Hz, which is at least 7 dB(A) higher than that of the case in which E_e equals 2 MPa. Consequently, the overall sound pressure level of the embedded rail track is 96.8 dB(A), 98.9 dB(A) and 97.8 dB(A) when E_e equals 2 MPa, 10 MPa and 20 MPa, respectively. This result indicates that increasing E_e is not an effective method for reducing the radiated noise of the track, and decreasing E_e from 5 MPa to 2 MPa can achieve a slight reduction, i.e., approximately 1 dB(A), for the radiated noise of the embedded rail track.

Similarly, Fig. 22 illustrates the decay rate of the embedded rail for different Young's modulus of the rail pad (called E_p below), and E_p in the current model of the embedded rail is 2 MPa. It can be seen that E_p have a significant influence on the decay rate. The peak frequencies of the decay rate stay consistent with an increase in E_p, and the decay rate rises with an increase in E_p in the frequency band below 1250 Hz. Particularly, in the frequency band below

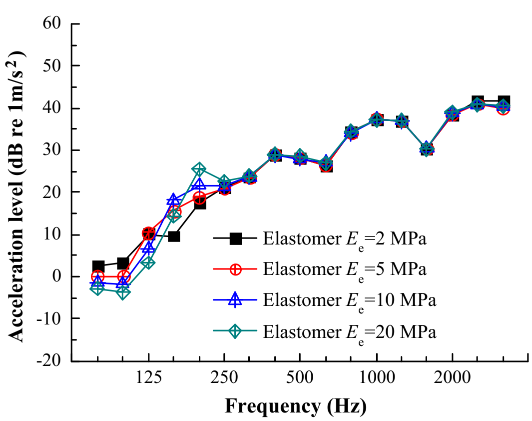

Fig. 19. Rail accelerations at the contact points for different E_e.

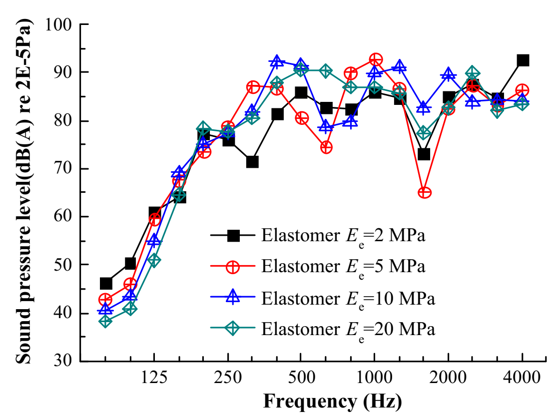

Fig. 21. Sound pressure spectra of the embedded rail track for different E_e.

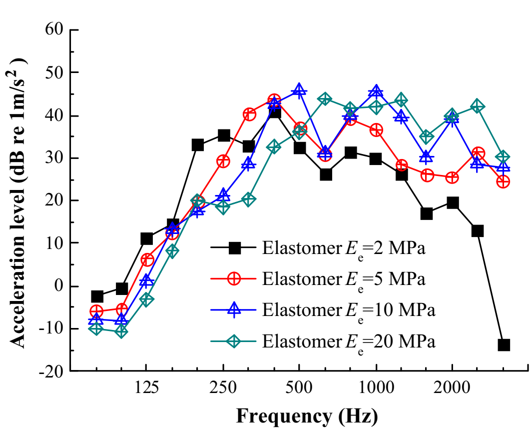

Fig. 20. Elastomer accelerations for the contact points with different E_e.

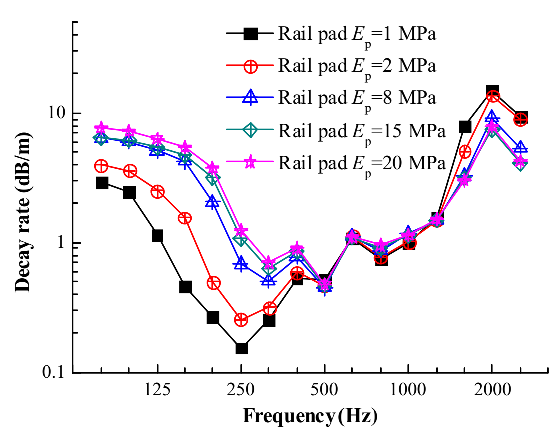

Fig. 22. Decay rate of the embedded rail for different E_p.

315 Hz, the increase in the decay rate is at least 3 dB/m when E_p increases from 1 MPa to 20 MPa whereas the decay rate decreases with an increase in E_p in the frequency band above 1250 Hz.

Figs. 23 and 24 illustrate the rail accelerations and the elastomer accelerations for different E_p, respectively. It can be seen that E_p has a slight influence on the rail acceleration and the elastomer acceleration. The rail vibration and the elastomer vibration decrease slightly with an increase in E_p below 160 Hz, and they increase slightly with an increase in E_p in the frequency band of 200–250 Hz. At 200 Hz, the rail acceleration and the elastomer acceleration increase 8 dB and 7 dB, respectively, when E_p increases from 1 MPa to 20 MPa. Furthermore, the elastomer vibration decreases slightly with an increase in E_p in the frequency band of 500–630 Hz, i.e., a reduction of approximately 2 dB when E_p increases from 1 MPa to 20 MPa.

Fig. 25 illustrates the sound pressure spectra of the embedded rail track for different E_p when the tram is running at 60 km/h. It can be seen from Fig. 25 that the sound pressure spectra of the embedded rail track vary with an increase in E_p, which is similar to the pattern of the rail and elastomer vibration. Consequently, the overall sound pressure level of the embedded rail track is 97.8 dB(A), 97.6 dB(A), 97.6 dB(A) and 97.6 dB(A) when E_p equals 1 MPa, 8 MPa, 15 MPa and 20 MPa, respectively. This result indicates that increasing E_p can slightly reduce the radiated noise of the embedded rail track; however, the reduction is quite limited.

Increasing the damping loss factors of the elastomer and the rail pad can slightly increase their decay rate and decrease the track vibration and the radiated noise. The damping loss factors of the elastomer and the rail pad used in the current model are 0.15. It is difficult to further increase the damping loss factor of these elastic materials, and their noise reduction is thus limited.

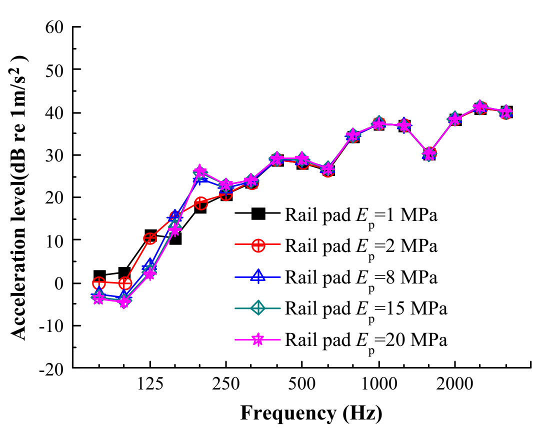

Fig. 23. Rail accelerations at the contact points for different E_p.

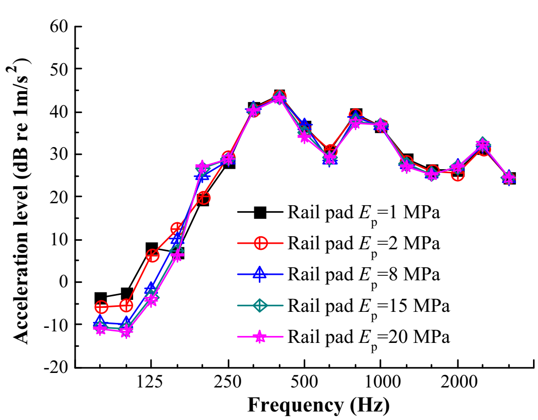

Fig. 24. Elastomer accelerations along with the contact points for different E_p.

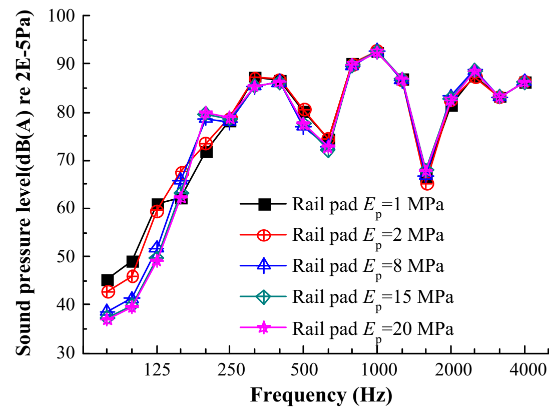

Fig. 25. Sound pressure level spectra of the embedded rail structure for different Young's modulus of the rail pad.

It can be determined that the vibration level of the rail and the elastomer significantly influences the radiated noise of the embedded rail track. By optimising the material parameters of the elastomer and the rail pad, the decay rates can be largely increased in the frequency band below 315 Hz, and optimising the material parameters of the elastomer and the rail pad has limited effects on reducing the radiated noise of the embedded rail track. The optimisation of the gutter cross-section of the embedded rail track may be a more effective method to achieve this target.

5.2. Gutter cross-section optimisation

Fig. 26 illustrates the comparison of the current cross-section and an optimised I-shaped cross-section of the gutter for the embedding rail. In the optimised structure, the elastomer is omitted between the rail and the rail pad so that the rail is supported by the rail pad directly, and the support stiffness of the rail in the vertical direction is slightly higher than that of the previous embedded rail structure. The I-shaped gutter cross-section can reduce the amount of elastomer used on both sides of the rail in the gutter. Therefore, the lateral stiffness of the embedded rail track increases, and the lateral stability of the rail increases. Furthermore, changing the gutter cross-section can increase the deformation and the energy dissipation of the elastomer when the rail vibrates in the gutter.

Fig. 27 illustrates a comparison of the decay rates for the embedded rail for the rectangular and the I-shaped gutter cross-sections. Figs. 28 and 29 depict the comparison of the rail and the elastomer accelerations of the embedded rail tracks for the rectangular and I-shaped gutter cross-sections, respectively. Additionally, Fig. 30 depicts the comparison of the sound pressure spectra of the embedded rail tracks for the two different gutter cross-sections. In these figures, the embedded rail track with the rectangular gutter cross-section is the un-optimised track structure (called un-optimised structure below), which uses the rail pad with a Young's modulus E_p = 2 MPa. Furthermore, the embedded rail track with the optimised I-shaped gutter cross-section uses the rail pad with the two types of Young's modulus, which are 2 MPa (called optimised structure I below) and 8 MPa (called optimised structure II below).

Comparing the black solid curve with the blue solid curve in each figure, it can be seen that the decay rate of the optimised structure I is higher than that of the un-optimised structure below 630 Hz, and it is lower than that of the un-optimised structure above 630 Hz. Below 200 Hz, the rail accelerations and elastomer

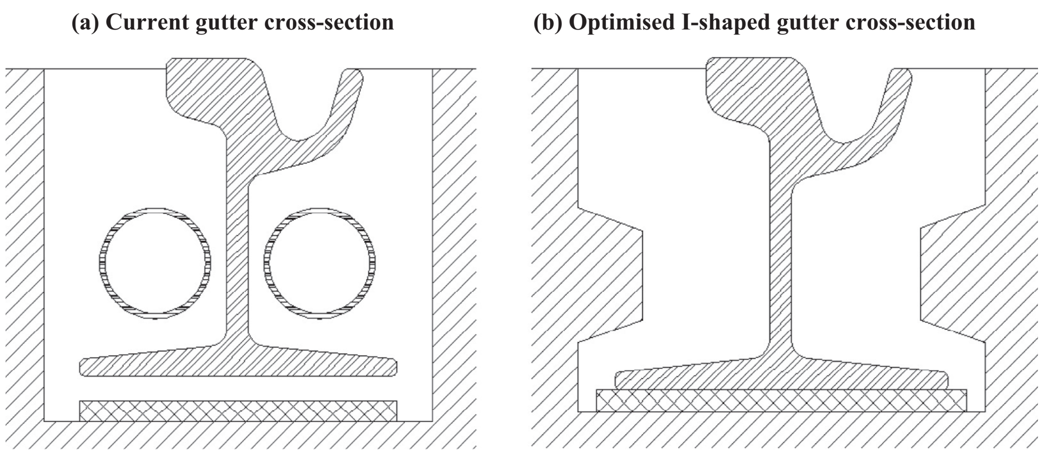

Fig. 26. Comparison of two gutter cross-sections for the embedded rail track.

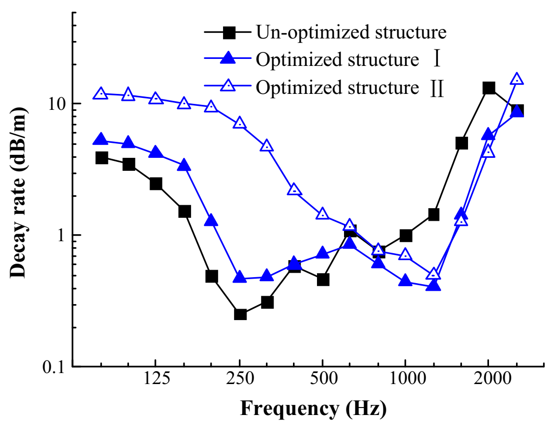

Fig. 27. Decay rate of the embedded rail track for the rectangular and I-shaped gutter cross-sections.

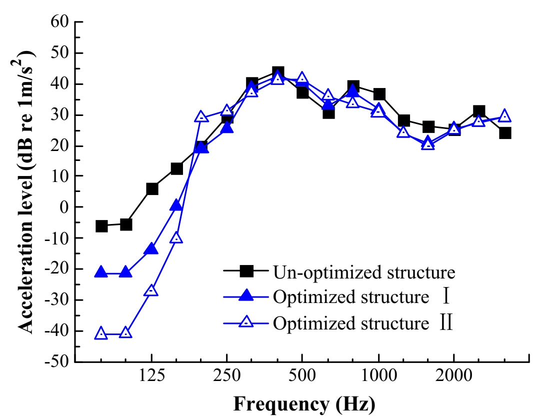

Fig. 29. Elastomer accelerations along with the contact points of the embedded rail track for the rectangular and I-shaped gutter cross-sections.

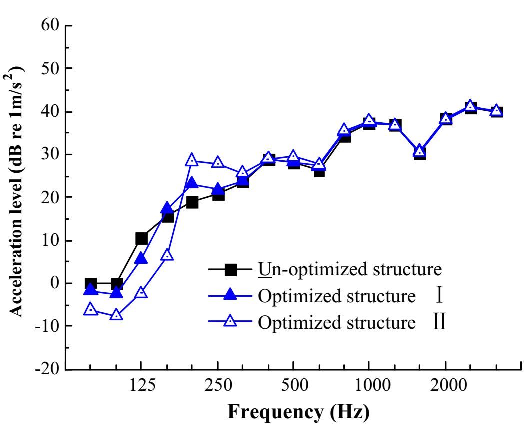

Fig. 28. Rail accelerations at the contact points of the embedded rail track for the rectangular and I-shaped gutter cross-sections.

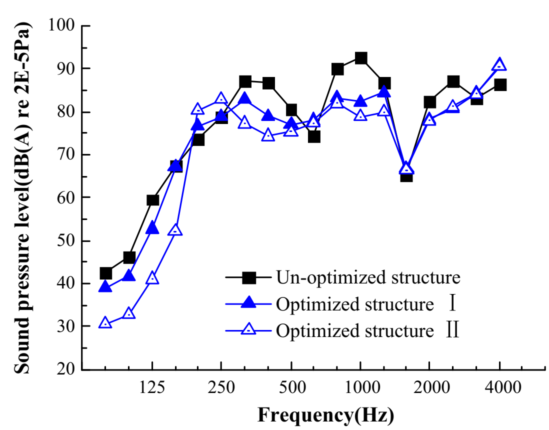

Fig. 30. Sound pressure spectra of the embedded rail track for the rectangular and I-shaped gutter cross-sections.

accelerations of the optimised structure I are considerably lower than those of the un-optimised structure; therefore, the sound pressure of the optimised structure I decreases at least 4 dB(A) in this frequency band compared with the un-optimised structure. In the frequency band of 800–1250 Hz, the rail acceleration of the optimised structure I is approximately the same as that of the un-optimised structure, the elastomer acceleration is between 2 and 5 dB lower than that of the un-optimised structure, and the sound pressure of the optimised structure I in this frequency band decreases primarily due to the elastomer vibration reduction, where the noise reduction can reach 2–10 dB(A).

The blue curve with empty triangles in each figure is the calculated result of the optimised structure II. It can be seen that changing the cross-section shape and increasing the Young's modulus of the rail pad simultaneously can significantly raise the decay rate below 1250 Hz whereas there is only a small change in the decay rate of the previous un-optimised structure when the Young's modulus of the elastomer or rail pad is changed. This result occurs because in the modified gutter, there is no elastomer between the rail foot and the rail pad but does exist in the original one. Thus, when the Young's modulus of the elastomer or rail pad is changed in the original structure, it has minimal effects on the overall stiffness. However, when both are changed in the modified gutter, it has more of an effect. Due to an increase in the Young's modulus of the rail pad, both the rail and elastomer accelerations further decrease below 200 Hz, and the elastomer acceleration further decreases in the frequency bands of 315–400 Hz, 800–1000 Hz. Therefore, there is a greater reduction in the sound pressure in the frequency band.

The gutter cross-section optimisation can effectively reduce the radiated noise of the embedded rail track. The embedded rail track with the I-shaped gutter cross-section (without changing material parameters, i.e., optimised structure I) can reduce the radiated noise by at least 3 dB(A), and changing the material parameters of the rail pad in the I-shaped gutter cross-section structure (optimised structure II) can result in an extra noise reduction of 1 dB(A).

This optimised structure has a better noise performance. Additionally, this structure can reduce the depth size of the track, which is particularly suitable for bridge lines and tunnel lines. However, this structure can considerably increase the difficulty in its construction to a certain extent. This type of track structure has been used in the bridge of the tram line in Xinjin, Chengdu suburb, Sichuan Province, China.

6. Conclusions

The decay rate, vibration and noise responses of an embedded rail track were measured. When a tram was running at 60 km/h, the overall sound pressure level of the wheel/rail rolling noise was 98.8 dB(A) inside the bogie, the measured noise reached its highest levels between 400 Hz and 1000 Hz, and the noise peaks in the frequency band of 400 Hz and 800 Hz were most likely caused by the radiated noise of the elastomer and the rail, respectively. The decay rate of the embedded rail was relatively lower in the frequency band of 100–1000 Hz, which most likely resulted in a longer track structure vibrating and radiating noise in this frequency range.

FE and BE models have been developed to calculate the decay rate, vibration and noise responses of the embedded rail track. These models can adequately predict the vibration and noise responses of the embedded rail track and optimise the track. These models have been validated using the measured results. The overall sound pressure level of the calculated track is 97.8 dB(A), which is slightly lower than the measured one. However, it can suitably reflect the frequency characteristics of noise for the track and wheel/rail rolling.

The optimisation focuses on the rail and elastomer vibration at the contact point and the track radiated noise above the contact point, and it does not include the effects of the decay rate on the radiated noise during a tram pass-by. Optimising the material parameters of the elastomer and the rail pad can only achieve a limited reduction in the radiated noise of the embedded rail track whereas optimising the gutter cross-section shape of the embedded rail track can significantly reduce the radiated noise of the embedded rail track. Using the I-shaped gutter cross-section in the embedded rail track can reduce the radiated noise by at least by 3 dB(A). In this type of structure, combining the material parameters with the gutter cross-section shape optimisation may be the most effective method to reduce the radiated noise. Increasing the Young's modulus of the rail pad in the embedded rail track with the I-shaped gutter cross-section can result in a radiated noise reduction of 4 dB(A).

Acknowledgements

This study was supported by the National Natural Science Foundation of China (No. U1434201), Ph.D. Programs Foundation of Ministry of Education of China (No. 20130184110005) and Scientific Research Foundation of State Key Laboratory of Traction Power, China (No. 2015TPL_T01). The authors wish to thank Gang Yang, Wei Li, Xing Du, Liang Lin, Qiang Zhou, Yabo Cao, Yuanpeng He and Yue Wu for their assistance in conducting the experiment, Jia Liu for her assistance with data analysis, and Jiong Luo for his assistance in the optimisation of the study.

References

[1] Carels P, Dirven S, Vogiatzis C, et al. Implementation of a PREFARAIL-COMFORT vibration isolation embedded track solution for Athens Tramway. In: Proceedings of the international conference on contemporary tram and LRT systems.
[2] Thompson D. Railway noise and vibration: mechanisms, modelling and means of control. Elsevier; 2008.
[3] Oostermeijer KH, Kok AWM. Dynamic behaviour of railway superstructures. HERON 2000;45(1).
[4] Nilsson CM, Jones CJC, Thompson DJ, et al. A waveguide finite element and boundary element approach to calculating the sound radiated by railway and tram rails. J Sound Vib 2009;321(3):813–36.
[5] Van Lier S. The vibro-acoustic modelling of slab track with embedded rails. J Sound Vib 2000;231(3):805–17.
[6] ISO 7626-5: Vibration and shock - experimental determination of mechanical mobility. Part. 5: measurement using impact excitation with an exciter which is not attached to the structure.
[7] EN 15461-2008: Railway applications — noise emission — characterisation of the dynamic properties of track sections for pass by noise measurements.
[8] Jones CJC, Thompson DJ, Diehl RJ. The use of decay rates to analyse the performance of railway track in rolling noise generation. J Sound Vib 2006;293(3):485–95.
[9] Remington PJ. Wheel/rail rolling noise, I: theoretical analysis. J Acoust Soc Am 1987;81:1805–23.
[10] Remington PJ. Wheel/rail noise, Part IV: rolling noise. J Sound Vib 1975;46:419–36.